A Dual-Mode 340-490 GHz Leaky-Wave-Antenna-Coupled Terahertz Detector with Power-balancing and Beam Monitoring

Min Liu, Xiaoyue Xia, Zhicheng Lin, Zijun Guo, Hao Guo, Yingxue Mo,
Jingyuan Zhang, Hiu Lok Tam, Kam Man Shum, and Chi Hou Chan
State Key Laboratory of Terahertz and Millimeter Waves,
City University of Hong Kong,
Hong Kong, SAR, China
m.liu347@cityu.edu.hk and eechic@cityu.edu.hk

***Abstract*—This paper presents a compact dual-mode 340-490 GHz terahertz (THz) detector for power-balancing monitoring, beam tracking, and imaging. Fabricated in a 65 nm CMOS process, the detector integrates a leaky-wave antenna (LWA) with two detection paths. Each path comprises a square-law detector and a gating transistor, while sharing a common output pad. Dual-mode operations are supported: the individual mode enables time-division readout of each path for power-balancing evaluation and incident-beam-direction estimation, whereas the simultaneous mode suppresses noise variation and enhances the signal-to-noise ratio (SNR). Measurements show a maximal responsivity (R_v) of 1.8k-11.2k V/W and a minimal noise-equivalent power (NEP) of 126-22.5 pW/sqrt(Hz) in individual mode, and a maximal R_v of 1.6k -9.5k V/W and a minimal NEP of 115-18.6 pW/sqrt(Hz) in simultaneous mode across the operation bandwidth. The proposed architecture thus offers self-monitoring, redundancy, and noise suppression, making it well-suited for THz/mm-wave imaging and sensing systems-on-chip.**

Keywords—terahertz, CMOS, square-law detector, leaky-wave antenna (LWA), power-balancing monitoring, gating transistor, individual, simultaneous, imaging.

I. Introduction

The terahertz (THz) frequency band (0.1–10 THz) offers promising applications in imaging, communications, radar, and nondestructive testing. As planar traveling-wave antennas, leaky-wave antennas (LWAs) are widely adopted in microwave and millimeter-wave systems due to their low profile, ease of integration, and high design flexibility. In practical scenarios, real-time monitoring of antenna power fluctuation is of significant importance—for example, to evaluate load-matching conditions, assess the uniformity of the transmitted power, enable system self-diagnosis, and support 2/3D imaging.

Conventional approaches typically employ square-law detectors at both antenna ends, with each output routed to an independent readout path. However, at THz frequencies, the limited number of chip pins and packaging constraints, particularly in focal-plane arrays (FPAs), make it difficult to implement dual-path independent outputs. A simple single-ended output inevitably loses the power information from the other end, preventing assessment of power balance and reducing system redundancy. Alternatively, adopting a time-division gating provides independent readouts but precludes noise reduction and bandwidth extension advantages afforded by simultaneous operation of both paths.

To address these limitations, this work proposes a dual-mode detector architecture operating from 340 GHz to 490 GHz. The individual mode could obtain both LWA port energy information, thus evaluating power balancing and incident beam direction, especially given the system's lack of redundancy. The simultaneous mode effectively compensates for signal fluctuations caused by scanning while improving the signal-to-noise ratio (SNR) by noise suppression.

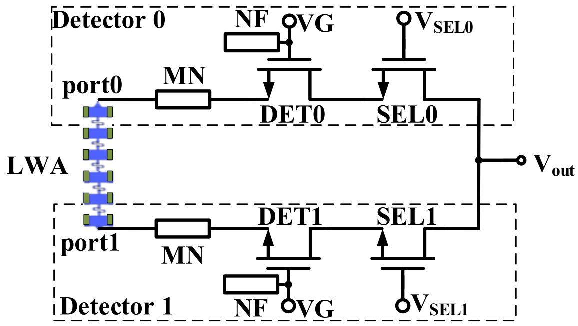

Fig. 1 Schematic of the proposed LWA-coupled detector.

II. Detector Implementation

Fig. 1 illustrates the architecture of the dual-mode LWA-based THz detector. The on-chip LWA consists of six periodically alternating transmission units (seen in Fig. 3), each integrating a substrate-integrated waveguide (SIW) with a microstrip line (MSL) [1]. THz energy is coupled into two square-law detectors (DET0 and DET1) via matching networks (MNs) [2-4], and the outputs are selectively routed by gating transistors (SEL0 and SEL1) to a shared pad. DET0 and DET1 are equipped with a notch filter (NF) at the gate.

The detector was fabricated in a 65 nm CMOS process. The AP layer serves as the radiating plane to reduce conductor losses and increase the radiation efficiency, while the M6 layer acts as the ground plane to suppress substrate parasitics and ensure stable electrical performance. Besides, the sidewall from the AP layer to M6 forms an AC ground path. The periodic SIW-MSL unit structure and dimensions are depicted in Figs. 2 (a) and (b), respectively. It is similar to the one reported in [1], which describes the LWA's working mechanism in detail. MNs increase the THz power received by the transistors from the antenna. SEL0/SEL1 transistors (4×0.28 μm/0.7 μm) enable dual-mode operation through ON/OFF switching, while DET0/DET1 transistors (1.2 μm/0.06 μm) integrate an NF at the gate to mitigate parasitic coupling in the individual mode. Leveraging the high-gain SIW-MSL structure, the detector achieves an impedance bandwidth of 124 GHz with nearly flat directivity exceeding 10 dBi. In measurements, the detector can operate from 340 to 490 GHz. Compared with other broadband antenna-coupled detectors [4,10], this design maintains high

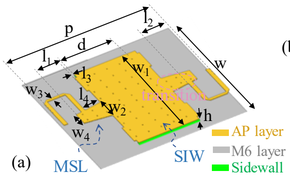

(b) Dimensions of the on-chip LWA

Par.	Val.(μm)	Par.	Val.(μm)	Par.	Val.(μm)
p	360	w	360	d	150
l_1	65	l_2	63.6	l_3	5
w_1	292	w_2	55	w_3	9.6
w_4	36	l_4	41	h	6.9

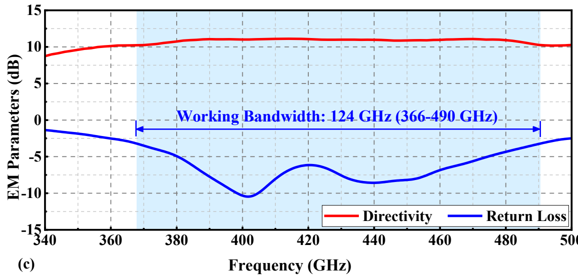

Fig. 2 (a) Configuration of the periodic SIW-MSL unit and (b) its detailed dimensions; (c) simulated electromagnetic parameters of the detector.

bandwidth without sacrificing efficiency.

For dual-mode operation, suppose the powers at the port0 and port1 terminals of LWA in Fig. 1(a) are P_0 and P_1, respectively. The two square-law detectors DET0 and DET1 are modeled as voltage sources V_0 and V_1, each with equal resistance R_d; their output voltages are proportional to the incident power: $V_x = R_{v,x} \cdot P_x$, (x = 0 or 1) where $R_{v,x}$ is the voltage responsivity. Each detector fans out its detected signal to an off-chip readout device via SEL0/SEL1 with an on-resistance R_{on} (identical for both switches) and an infinite off-resistance. The input impedance of the readout device is R_L, which is much larger than $R_d + R_{on}$ (Generally 100 MΩ). All noise sources are assumed uncorrelated. The dominant noise contributions are: thermal noise of DET0 and DET1 ($n_d = sqrt(4kTR_dB)$) and thermal noise of SEL0 and SEL1 ($n_d = sqrt(4kTR_{on}B)$), where k is Boltzmann's constant, T is the absolute temperature, and B is the measurement bandwidth.

In the individual equivalent mode shown in Fig. 3(a), SEL0 or SEL1 is activated independently. Owing to $R_L \gg R_d + R_{on}$, yielding a readout voltage $V_{out,single}$, accompanied by noise $V_{n,single}$:

$$V_{out,single} = \frac{R_L}{R_d+R_{on}+R_L} \cdot V_0 \approx V_0 \tag{1}$$

$$V_{n,single} = \mathrm{sqrt}(4\mathrm{kT}(R_d + R_{on}) \cdot \mathrm{B}) \tag{2}$$

Note that the readout device noise is negligible. Hence, the signal-to-noise ratio (SNR) in this mode is

$$SNR_{single} = \frac{V_0^2}{4\mathrm{kT}(R_d+R_{on})\cdot \mathrm{B}} \tag{3}$$

In simultaneous mode, both paths are active in parallel. The equivalent circuit is presented in Fig. 3(b); the parallel connection results in an equal resistance of $(R_d + R_{on})/2$, yielding an averaged output of DET0 and DET1:

$$V_{out,both} \approx (V_0 + V_1)/2 \tag{4}$$

Since the two paths are symmetric, the mean-square output noise becomes

$$V_{n,both} = \mathrm{sqrt}(2\mathrm{kT}(R_d + R_{on}) \cdot \mathrm{B}) \tag{5}$$

Here, the readout device noise is negligible. Consequently, the SNR for simultaneous mode is

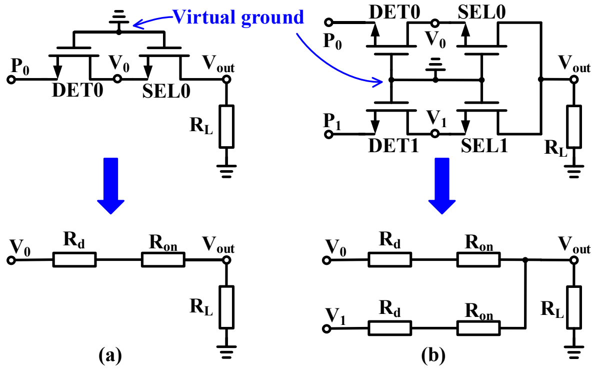

Fig. 3 (a) Equivalent circuit of individual mode and (b) simultaneous mode.

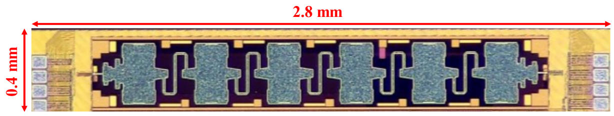

Fig. 4 Chip micrograph.

$$SNR_{both} = \frac{((V_0+V_1)/2)^2}{2\mathrm{kT}(R_d+R_{on})\cdot \mathrm{B}} \tag{6}$$

If the signals DET0 and DET1 are equal ($V_0 = V_b = V$), the SNR can be simplified to

$$SNR_{both} = \frac{V^2}{2\mathrm{kT}(R_d+R_{on})\cdot \mathrm{B}} \tag{7}$$

Compared to the individual mode, the SNR improvement factor of the simultaneous mode over the single mode is

$$\frac{SNR_{both}}{SNR_{single}} = \frac{4\mathrm{kT}(R_d+R_{on})\cdot \mathrm{B}}{2\mathrm{kT}(R_d+R_{on})\cdot \mathrm{B}} \approx 2 \tag{8}$$

Which is around a 3dB improvement. Nevertheless, when the signals V_0 and V_1 are unbalanced, this value is less than the smaller of the two, limiting noise reduction.

III. Experimental Results

To validate the proposed architecture, a prototype detector was fabricated and characterized. Fig. 4 reveals the chip micrograph. The dual-mode LWA detector was fabricated in 65 nm CMOS and occupies an active area of 0.4 × 2.8 mm^2. As illustrated in Fig. 5, characterization was performed using an amplitude-modulated source with a VDI WR-2.2 amplifier-multiplier chain, placed 77 mm from the detector. A lock-in amplifier synchronized with the VDI source enabled demodulation of the detected signals. The Agilent E8257D signal generator provided an injection signal to the source, which was then multiplied by 36 to produce a modulated signal spanning 325-500 GHz.

A. Responsivity(R_v) and NEP

According to Friis transmission equation, the input power P_{in} to the detector can be calculated from the irradiance and the effective receiver antenna area A_{eff} at a distance d as

$$P_{in} = \frac{P_{rad}\cdot G_{rad}}{4\pi d^2} \cdot A_{eff} \tag{9}$$

Where P_{rad} is the radiated source power at the antenna port, G_{rad} the source antenna gain (25 dBi), and $A_{eff} = D_{LWA} \cdot \lambda^2/4\pi$ the effective area of the LWA with directivity

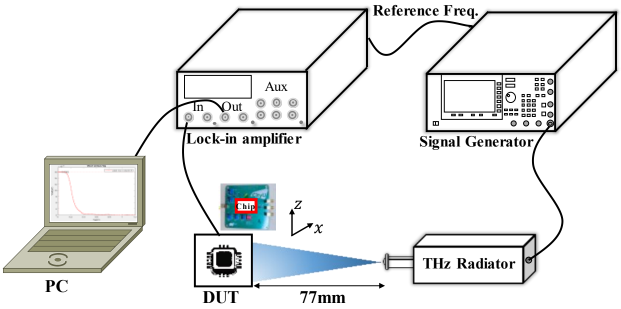

Fig. 5 Detector experimental setup with lock-in techniques.

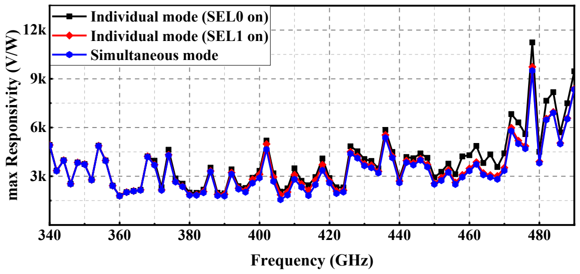

Fig. 6 Measured maximum responsivity versus frequency at 10.24 kHz modulated frequencies.

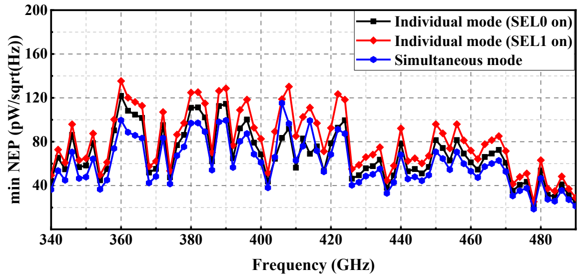

Fig. 7 Measured minimum NEP versus frequency at 10.24 kHz modulated frequencies.

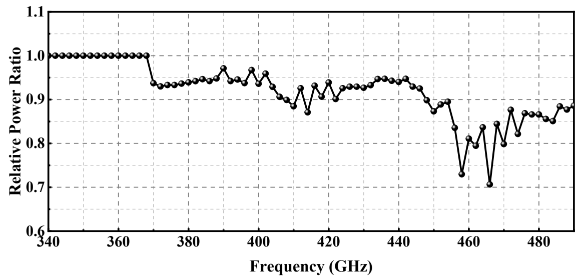

Fig. 8 Measured relative power ratio under two individual modes (SEL1 on and SEL0 on, corresponding to power detection at port0 and port1).

D_{LWA}. Once P_{in} is known, the responsivity $R_v = V_{out}/P_{in}$ and $NEP = V_{noise}/R_v$ can be derived from the DC measurements of the detected output signal V_{out} and spot noise V_{noise}.

Measurements across 340–490 GHz in Fig. 6 displayed an optimal R_v of 11.2 kV/W at 478 GHz in individual mode and 9.5 kV/W at 478 GHz in simultaneous mode. In particular, the available P_{in} of only -44.3 to -35.9 dBm was measured with an absolute-power calorimeter according to equation (9). Fig.7 presents the minimal NEP versus frequency. The optimal NEP is 22.5 pW/sqrt(Hz) at 478 GHz in individual mode and 18.6 pW/sqrt(Hz) in simultaneous mode. Note that all data were measured at a modulation frequency of 10.24 kHz.

B. Power-Balancing and Beam Monitoring

In individual mode, the outputs from port0 (SEL0 on) and port1 (SEL1 on) were compared to evaluate power consistency. The extracted relative power ratio is shown in Fig. 8. The variation remains within 10% over the 340-450 GHz band, which is acceptable for the design. At higher frequencies, where the LWA beam is steered to larger angles, even a slight deviation in the incident wave can induce asymmetry in the radiation distribution, leading to a progressively larger power difference between the two detectors.

By employing two distinct individual modes and recording power by time-division readout, the incident beam direction can be effectively monitored. Fig. 9 shows the relative power difference P_{SEL0}-P_{SEL1} versus travel distance along the x-axis at four different frequencies. When the incident wave deviates from the LWA's beam center, the P_{SEL0}-P_{SEL1} difference becomes clear. If P_{SEL0}-P_{SEL1} is negative, the direction of the source should be shifted toward the SEL0 terminal; otherwise, it should be shifted toward the SEL1 terminal.

C. Signal-to-Noise Ratio (SNR) Comparison

Fig. 10 measured the SNR in dual-mode operation. Simultaneous mode yields a flatter SNR than the individual mode due to lower total impedance. Meanwhile, the simultaneous mode provided an average SNR improvement of approximately 2.8 dB over the individual mode, consistent with the theoretical predictions in Section II. Minor asymmetry between the two individual modes resulted in a 1.3 dB variation, attributed to structural or matching variations.

D. Imaging Capability

To assess the imaging capability of the LWA detector, we set up a transmission-imaging platform as shown in Fig. 11. A 0.9 cm-wide cutter blade was chosen as the sample. The image was raster-scanned at 440 GHz. Even though there are no optical elements, the defect of the blade is distinguishable.

IV. CONCLUSIONS

In this work, we presented a compact 340-490 GHz dual-mode LWA-coupled THz detector in a 65nm CMOS process. Table I provides a comprehensive comparison between the proposed LWA detector and other THz detector works. The LWA detector surpasses prior THz detectors in multiple functions while maintaining competitive R_v and NEP performance. Moreover, by integrating two square-law detectors with shared output gating, the proposed architecture enables both power-balancing and incident-beam-direction monitoring in individual mode, while simultaneous mode provides effective noise suppression and improves the SNR. Future work will explore array-level integration and adaptive beam monitoring, extending the detector toward compact, intelligent THz imaging and sensing systems-on-chip.

TABLE I. STATE-OF-THE-ART OF THE INTEGRATED THZ DETECTORS

Ref.	This work	NC'19 [6]	ISSCC'21 [7]	TMTT'22 [8]	TMTT'22 [9]	TTST'24 [4]	TTST'26 [10]
Process	65 nm CMOS	65 nm CMOS	130 nm CMOS	130 nm SiGe	65 nm CMOS	65 nm CMOS	65 nm CMOS
Bandwidth (THz) #	0.34-0.49	0.1-0.35	0.46-0.75	[2]0.25-0.6	0.3	0.075-1.1	[3]0.247-0.34
Max R_v* (V/W)	[4]1.8k-11.2k [5]1.6k-9.5k	703, 0.1 THz	[1]35k, 0.6 THz	7k-9k	425	250-1.4k	[3]180-1050
Min NEP (pW/√Hz)	[4]126-22.5 [5]115-18.6	20.4, 0.1 THz	262, 0.6 THz	2.2-1.9	26.4	290-17	75, 0.32 THz
Antenna Type	LWA	Log-periodic + Si lens	Loop + Si lens	Wire ring + Si lens	Patch	8-loop + Si lens	Bow tie
Modulated Freq. (Hz)	10.24k	-	40k	100k	500k	367	250
Operation Mode†	Individual & simultaneous	Simultaneous	Simultaneous	Simultaneous	Simultaneous	Simultaneous	Individual

-3dB impedance bandwidth. || * Normalized responsivity excluding the gain of on-chip/off-chip amplifier.

† Simultaneous mode refers to the detector with a differential-transistor configuration, while individual means a single-transistor detecting configuration.

[1] with an integrated amplifier of 128-dB gain. || [2] 3-dB bandwidth is estimated from the reported R_v versus frequency curve. || [3] estimated from the reported R_v versus frequency curve

[4] Max. responsivity and min. NEP measured in individual mode. || [5]Max. responsivity and min. NEP measured in simultaneous mode

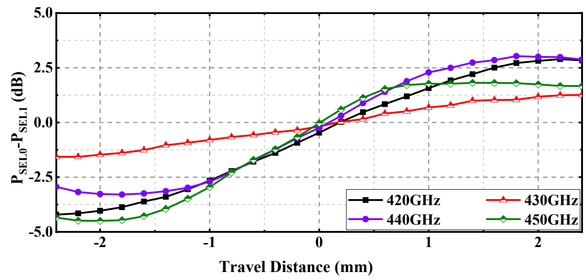

Fig. 9 Measured relative power difference versus travel distance along the x-axis at various frequencies.

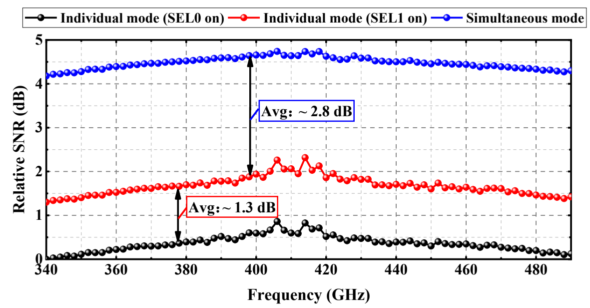

Fig. 10 Measured SNR versus frequency at 0.1V gate bias.

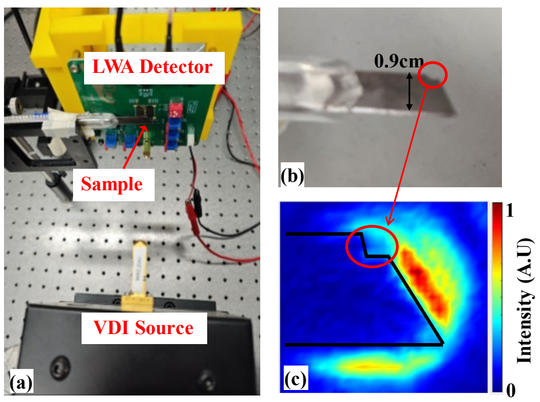

Fig. 11 (a) Imaging platform; (b) the imaging target (0.9 cm-width cutter blade) and its (c) raster-scanned image at 440 GHz.

ACKNOWLEDGMENT

The authors would like to thank Dr. Ka Fai Chan for his assistance with the THz measurements. This work was supported by the Hong Kong Research Grants Council General Research Fund under Grant CityU 11214123 and the Hong Kong Research Grants Council Collaborative Research Fund under Grant C1009-22G. The corresponding author is Prof. Chi Hou Chan (email: eechic@cityu.edu.hk).

REFERENCES

[1] X. Xia et al., "On-Chip Leaky-Wave Antenna With 220-500 GHz Bandwidth and 128° Beam Scanning in 65-nm CMOS Process," *IEEE Trans. Antennas Propag.*, vol. 74, no. 4, pp. 3010-3023, April 2026.

[2] M. Liu et al., "A 16.4kPixel 3.08-to-3.86THz Digital Real-Time CMOS Image Sensor with 73dB Dynamic Range," in Proc. *IEEE Int. Solid-State Circuits Conf.*, San Francisco, CA, USA, 2023, pp. 4–6.

[3] M. Liu et al., "A 3 THz CMOS Image Sensor," *IEEE J. Solid-State Circuits*, vol. 59, no. 9, pp. 2934–2947, Sept. 2024.

[4] Z.-Y. Liu, L.-Y. Liu, J. Yang, and N.-J. Wu, "A CMOS fully integrated 860-GHz terahertz sensor," *IEEE Trans. Terahertz Sci. Technol.*, vol. 7, no. 4, pp. 455–465, Jul. 2017.

[5] Z.-Y. Liu, F. Qi, Y.-L. Wang, P.-X. Liu, and W.-F. Li, "A Multiband Terahertz Detector in 65-nm CMOS for Spectroscopic Imaging," *IEEE Trans. Terahertz Sci. Technol.*, vol. 14, no. 6, pp. 781-790, Nov. 2024.

[6] X. Wu, H. Lu, and K. Sengupta, "Programmable terahertz chip-scale sensing interface with direct digital reconfiguration at sub-wavelength scales," *Nature Commun.*, vol. 10, Jun. 2019, Art. no. 2722.

[7] R. Jain et al., "A 32 × 32 pixel 0.46-to-0.75 THz light-field camera SoC in 0.13 μm CMOS," in Proc. *IEEE Int. Solid-State Circuits Conf.*, 2021, pp. 484–486.

[8] M. Andree, J. Grzyb, R. Jain, B. Heinemann, and U. R. Pfeiffer, "Broadband modeling, analysis, and characterization of SiGe HBT terahertz direct detectors," *IEEE Trans. Microw. Theory Techn.*, vol. 70, no. 2, pp. 1314–1333, Feb. 2022.

[9] K. Song, D. Kim, J. Kim, J. Yoo, W. Keum, and J. -S. Rieh, "A Scalable 300-GHz Multichip Stitched CMOS Detector Array," *IEEE Trans. Microw. Theory Techn.*, vol. 70, no. 3, pp. 1797-1809, March 2022.

[10] G. Quarta, M. Perenzoni, L. Gasparini, and S. D'Amico, "Autozeroed bias circuit to enhance gain and uniformity of THz FET detectors for imaging," *IEEE Trans. Terahertz Sci. Technol.*, doi: 10.1109/TTHZ.2026.3679243, in press.